# Frequency Response of Power System Load-Side Asynchronous Motors Considering ROCOF

Yunlu LI, Zhouying LIU, Guotao SONG, and Jinliang HUANG

***Abstract*—Load-side asynchronous motors (AMs) inherently lower rotor speeds during frequency dips, reducing active power absorption and delivering vital inertial support. However, existing frequency regulation strategies overlook the dual objectives, neglecting frequency response adaptability and induction motor operational stability. This paper proposes a segmented rate of change of frequency (ROCOF) control strategy for AM-based primary frequency regulation. First, ROCOF is divided into distinct intervals. In low ROCOF regions, AMs leverage natural electromechanical transients to stabilize frequency. In medium-high ROCOF regions, coordinated control AMs, which incorporate with variable-frequency asynchronous motors (VFAMs) using adaptive droop coefficients are deployed. This coordination maximizes frequency support while maintaining VFAMs' stability. An adaptive model predictive control (MPC) framework is then designed to optimize dynamic frequency tracking for VFAMs. Simulations and hardware-in-the-loop (HIL) validate the strategy under uncertain system disturbances. Compared to conventional methods, the proposed approach elevates frequency nadirs, confirming enhanced transient performance, while maintaining normal operating conditions.**

***Index Terms*—Adaptive parameter adjustment, asynchronous motors, frequency regulation, load-side response, power balance.**

## I. Introduction

THE integration of renewable energy sources (RES) into power grids poses critical frequency stability challenges, stemming from their inherent stochasticity and variability [1]. Modern systems with high RES penetration and pronounced power fluctuations increasingly expose the limitations of conventional generation-side inertial control frameworks in meeting stringent frequency safety requirements. Evidence confirms that generation-side regulation alone inadequately mitigates frequency deviations in high-RES scenarios, necessitating coordinated utilization of supply and demand-side resources. Strategic deployment of demand-side flexibility with energy storage systems (ESS) facilitates bidirectional grid interactions [2]–[4], enhancing resilience. This integration enhances operational robustness while advancing sustainable grid modernization [5], [6].

Compared to generation-side power ramping for frequency nadir mitigation, load-side regulation demonstrates superior dynamic responsiveness and proactive control. To address inertia-deficient frequency instability in high-renewable systems, current studies focus on decentralized control mechanisms for load-side primary frequency regulation, particularly targeting stochastic large-scale loads as demonstrated in [7]–[9]. Specifically, [10] proposes aggregating air-conditioning loads for frequency regulation, enhancing frequency control. [11] proposes the electro-thermal coupling characteristics and decentralized control strategies of residential heat pump clusters for dynamic frequency regulation. [12] proposes hierarchical coordination and temperature-power coupling models to tap into the frequency regulation potential of residential HVAC clusters. [13] applies virtual synchronous generator (VSG) technology to electric vehicle charging stations, transforming passive loads into active frequency regulation units while balancing charging needs and grid support. [14] proposes the dynamic adaptability of electrified railway loads with energy storage systems to provide inertia support and enhance primary frequency regulation while meeting transportation service quality requirements. However, these research efforts fall short of fully addressing challenges such as load diversity, stochastic user behavior, and communication delays.

Industrial loads, with their rapid response and significant adjustability, have been studied for frequency regulation. [15] proposes the dynamic adaptability of high-energy-consumption loads like aluminum electrolysis and electric arc furnaces in isolated high-wind-penetration grids for frequency regulation through field experiments in industrial settings, although the study is confined to specific industrial processes. [16] devises a model predictive control (MPC) based methodology for aluminum electrolysis loads, substantially enhancing frequency stability. Additionally, [17] dynamically regulates electrolytic load power consumption to compensate for frequency deviations and explores economic mechanisms for their market participation, but ignores operational safety requirements. [18] presents a source-load-storage coordinated frequency regulation method with abandoned mine pumped storage, using distributed MPC to enhance dynamic performance, but faces excessive operational complexity and economic costs.

The existing literature has made certain contributions to

Manuscript received March 30, 2025; revised October 29, 2025; accepted November 17, 2025. Date of publication March 30, 2026; date of current version January 13, 2026. This work was supported in part by Liaoning Provincial Joint Science and Technology Program-General Program under the grant 2025-MSLH-532. (*Corresponding author: Yunlu Li.*)

All authors are with the School of Electrical Engineering, Shenyang University of Technology, Shenyang 110819, China (e-mail: liyunlu@sut.edu.cn; Lzy0619@smail.sut.edu.cn; sgt@smail.sut.edu.cn; HJL@smail.sut.edu.cn).

Digital Object Identifier 10.24295/CPSSTPEA.2025.00039

load-side frequency modulation, but most research focuses on single-dimension control and neglects the heterogeneity of load types. As the most common industrial load type [19], asynchronous motors (AMs) offer large regulation capacity and fast response speed, which can significantly enhance the frequency response characteristics of power systems [20]. In particular, variable-frequency asynchronous motors (VFAMs) can effectively support frequency regulation requirements after the high-proportion integration of renewable energy due to their rapid response characteristics [21]. However, conventional AMs are constrained by their nonlinear inertial release characteristics, resulting in a time-varying decay feature of their frequency response capacity. Meanwhile, VFAM may cause sub-synchronous frequency instability due to the aliasing of electromechanical oscillation modes caused by rigid speed constraints. This study overcomes the limitations inherent in discrete control by proposing a dynamic coordination framework for heterogeneous systems, effectively resolving the energy mismatch challenges associated with conventional single-response strategies.

Based on the mechanical characteristics of the coordinated frequency response system for AM and VFAM (AM-VFAM) and the frequency response requirements of the power system, this paper improves the frequency response strategy of AM-VFAM from two dimensions: the load-side frequency response structure and the frequency response support mode of AM-VFAM. A control strategy for AM-VFAM based on the rate of change of frequency (ROCOF) is proposed. A MPC method with adaptive weights is adopted to ensure that the MPC can adaptively adjust to system parameter changes under uncertain system disturbances, to guarantee the optimal frequency control effect. The principal contributions of this work are summarized as follows:

(a) Based on the changes in system frequency response, the ROCOF is divided into three intervals. In Interval I, conventional AMs respond to system frequency through their electromechanical transient characteristics. In Intervals II and III (medium and high ROCOF intervals), conventional AMs are coordinated with VFAMs with dynamic droop coefficients to achieve the frequency nadir while ensuring the normal operation of VFAMs.

(b) A MPC method with adaptive weights is adopted to ensure that the MPC can adaptively adjust to system parameter changes under uncertain system disturbances, to guarantee the optimal frequency control effect.

Section II introduces the AM-VFAM frequency response model. Section III presents the three-interval division framework. Section IV introduces the adaptive MPC with online weight adjustment. Section V provides case studies and analysis. Section VI concludes the paper.

## II. Frequency Model of AM-VFAM

Both AMs and VFAMs exhibit certain frequency modulation effects in frequency response. In this section, the frequency response capability of AM will be analyzed, and a model for the frequency response of VFAM will be established.

### *A. Active Power Support Capability of AM*

The load-side conventional AM, typically composed of fan and pump loads, forms a nonlinear coupled system [22]. Connected directly to the grid, it sees its slip rate affected by system frequency changes in the initial frequency response stage, causing electromagnetic power reduction and presenting a smaller effective inertia to the system. Subsequently, the kinetic energy stored in the rotor is gradually released, resulting in a larger effective inertia. Because of the frequency coupling between the AM and the system, its response during the speed regulation process is relatively fast, enabling it to effectively deal with the system's ROCOF and significantly contributing to system frequency stability.

### *B. Frequency Response Modeling of VFAM*

VFAM cannot inherently participate in demand response and require integrated frequency control modules for frequency-based demand response [23]. Through the variable frequency drive, the reference speed is altered to modify the mechanical energy consumption of the variable frequency motor, facilitating its participation in frequency-based demand response [15]. Based on the constant load torque of the motor, the following relationship can be derived

$$n_{r2} = n_{r1} - \Delta n_r \tag{1}$$

$$P_{m2} = P_{m1} - \Delta P_m \tag{2}$$

$$\Delta n_r = k_n n_{r1} \tag{3}$$

$$\Delta P_m = k_p P_{m1} \tag{4}$$

where $n_{r1}$, $n_{r2}$, $\Delta n_r$, $P_{m1}$, $P_{m2}$, and $\Delta P_m$ are the mechanical pre-speed, post-speed, speed change value, pre-speed change power, post-speed change power, and power change value, respectively. $k_n$ and $k_p$ are the proportional coefficient of the speed change and the power change relative to the pre-speed-change mechanical power.

For constant-torque loads, the following relationship can be derived based on the motor's constant-load torque.

$$(P_{m1} - k_p P_{m1})(n_{r1} - k_n n_{r1})^{-1} = P_{m1} n_{r1}^{-1} \tag{5}$$

$$k_p = k_n \tag{6}$$

When the VFAM is under constant torque load, the motor speed varies in the same proportion as the mechanical power. To participate in frequency response by changing the active power consumed by the VFAM, The power loss variation of the VFAM should be considered. the following equation is obtained

$$\Delta P_{DR} = \Delta P_m + \Delta P_{loss} \tag{7}$$

$$\Delta P_{DR} \approx k_p P_{m1} + k_p P_{lossl} \tag{8}$$

where $\Delta P_{DR}$, $\Delta P_{loss}$, and $P_{lossl}$ are the power reduction for motor frequency regulation, power loss variation, and pre-speed-change power loss component, respectively.

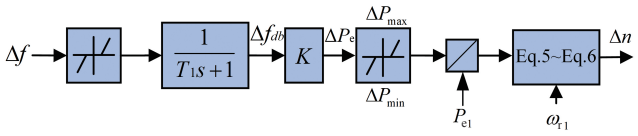


Fig. 1. Frequency response block diagram of VFAM.

Converting $P_{lossl}$ to $\Delta P_{loss}$, approximated as a portion of $P_{lossl}$, allows calculating an approximate $\Delta P_{loss}$. (8) can then be written as

$$k_p \approx \frac{\Delta P_{DR}}{P_{ml} + P_{loss}} = \frac{\Delta P_{DR}}{P_{el}} \tag{9}$$

The frequency response control method for VFAM is shown in the Fig. 1.

where $\Delta f$, $K$, and $\Delta P_e$ are frequency change, droop gain, and power change of the VFAM, respectively. The filtering time constant is $T_1$. $\Delta P_{min}$, $\Delta P_{max}$, $P_{el}$, and $\omega_{r1}$ are the maximum adjustable power, minimum adjustable power, initial power of the motor and angular velocity of the motor, respectively.

In the Fig. 1, filtering is first performed, and the VFAM obtains the same active frequency droop characteristics as the synchronous motor through the droop gain, thus, the corresponding power change of the VFAM can be calculated. To ensure the stable operation of the VFAM under normal working conditions, its maximum power change is limited to the range $[\Delta P_{min}, \Delta P_{max}]$. The value obtained by dividing the power response by the initial motor power is used as the input of the subsequent module and $\omega_{r1}$ is substituted into (5) and (6) to obtain the reduced speed corresponding to the reduced power, so that the VFAM can adjust its speed according to the change of system frequency, thereby achieving the frequency response requirement.

## III. Primary Frequency Response Based on ROCOF

### *A. ROCOF and Frequency Response Range Division*

After the VFAM uses the simulated synchronous motor droop coefficient to participate in frequency response, the dynamic response equation of the system is equivalent to [24]

$$2H_s \frac{df}{dt} = P_{Gi} - P_{asy} - P_{load} \tag{10}$$

where $H_s$ is the system equivalent inertia time constant, $f$ is the system frequency, $P_{Gi}$ and $P_{asy}$ are the power generated by the synchronous generator and absorbed by the AM respectively. $P_{load}$ is the load power fluctuations. Linearizing (10) and considering the power imbalance $\Delta P_u$, the initial ROCOF of the system can be obtained as

$$F(t_0) = \frac{d\Delta f}{dt}\Big|_{t=t_0} = -\frac{\Delta P_u}{2H_s} \tag{11}$$

where $F(t_0)$ is the ROCOF of the system at the time $t_0$, $F(t_0)$ is proportional to $\Delta P_u$. The ROCOF is segmented into distinct intervals defined by the proposed formula, enabling targeted control strategies to enhance VFAM's frequency regulation performance.

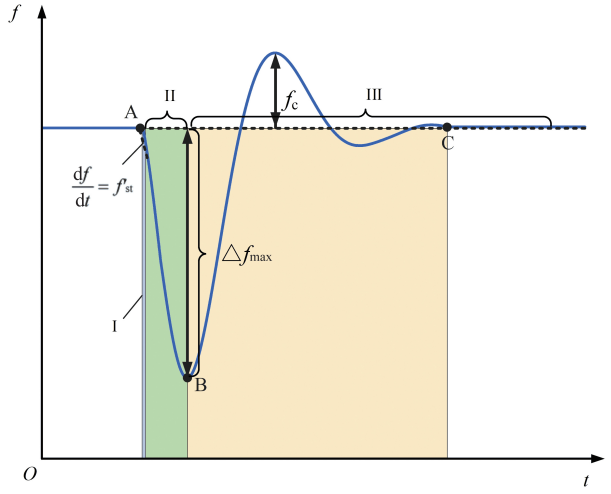


Fig. 2. Frequency response curve based on the intervals divided by ROCOF.

### *B. ROCOF and Frequency Response Range Division Principle*

The frequency deviation limit under normal operating conditions of the power system is ±0.2 Hz. Furthermore, a threshold $F_{st}$ is set for the system's steady-state frequency deviation $\Delta f_{st}$, and different frequency response zones are divided based on the severity of the disturbance.

Therefore, its correlation with ROCOF should be utilized to transform the relevant interval to the ROCOF domain [25]. Assuming that the power imbalance in steady state is borne by the synchronous generator set, its active output increment is

$$\Delta P_G = -\frac{\Delta f_{st}}{R_s} \tag{12}$$

where $R_s$ is the equivalent regulation coefficient of the system, satisfying, $R_s = R_G/(1 - p)$. When the system frequency deviation is $F_{st}$, the corresponding maximum active output of the synchronous machine $\Delta P_{unb,max}$ is the critical power imbalance of the system

$$\Delta P_{unb,max} = \Delta P_{G,max} = \frac{F_{st}}{R_s} \tag{13}$$

where $\Delta P_{G,max}$ represents the maximum active power output of the power system generator. Substituting (13) into (10), the $\Delta P_G$ corresponding initial frequency change is

$$f'_{st} = -\frac{\Delta P_{unb,max}}{2H_{eq}} = -\frac{F_{st}}{2H_{eq}R_s} \tag{14}$$

Therefore, according to the frequency drop caused by system disturbance, ROCOF can be divided into three intervals, as shown in Fig. 2 and Table I.

TABLE I
THE FREQUENCY VARIATION CHARACTERISTICS OF ROCOF INTERVAL DIVISION

| Interval | Interval Range | Frequency Characteristics | | |
|---|---|---|---|---|
| | | Stage | $\Delta f$ | ROCOF |
| I | $df/dt < f'_{st}$ | Initial descent | Reduced | Enhanced |
| II | $f'_{st} \leqslant df/dt < 0$ | Frequency minimum | Incremental transition | Decremental transition |
| III | $0 \leqslant df/dt$ | Frequency recovery | Decremental transition | Positive |

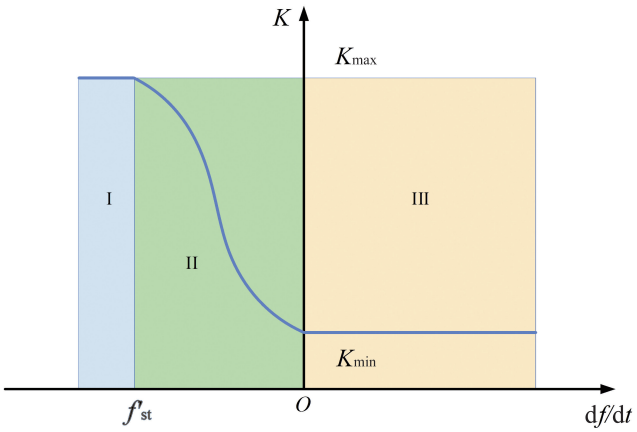


Fig. 3. Butterworth-type droop coefficient curve.

where $\Delta f_{max}$, Point A, Point B, and Point C are the maximum frequency deviation, the quasi-steady-state operating point of the frequency before the disturbance occurs, the lowest point of the frequency after the disturbance occurs, and the quasi-steady-state operating point of the system frequency after the disturbance occurs, respectively.

Fig. 2 is the typical frequency response curve under a system power shortage. Table I shows the frequency variation characteristics of ROCOF interval division.

### *C. Adaptive Droop Coefficient via ROCOF-Oriented Interval Segmentation*

According to the above analysis, the frequency dynamics after the system disturbance can be divided into Interval I, Interval II, and Interval III. For different frequency dynamic intervals, the VFAM adopts different droop coefficient strategies [26].

(I) The droop coefficient is denoted as $K_{max}$. In the absence of the VFAM, the system's dynamic response is investigated. In this configuration, the AM primarily provides power support to the system.

(II) The VFAM participates in the frequency response, and the droop coefficient $K_{max}$ gradually decreases from the maximum droop coefficient of the system as ROCOF decreases, preventing the VFAM from over-decelerating while increasing the frequency nadir.

(III) As the system frequency stabilizes, the droop coefficient is dynamically adjusted to a lower value. To maximize participation in system frequency response while minimizing impact on VFAM's normal operation.

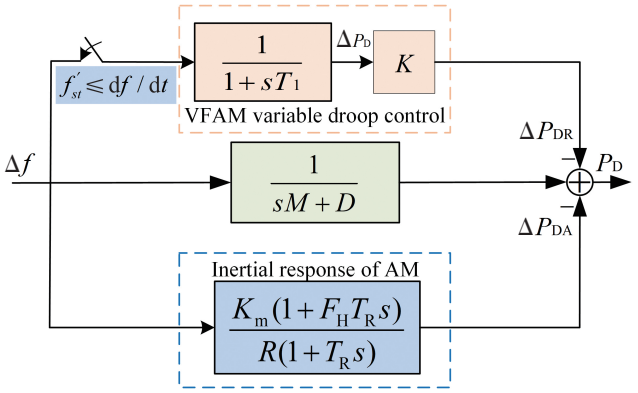


Fig. 4. System frequency response block diagram.

To mitigate the secondary effects of the frequency conversion module of the VFAM on the system frequency caused by sudden changes, and to reduce fatigue wear on the motor's internal components, this paper employs a fifth-order Butterworth function to ensure a smooth transition of the droop coefficient [27] (see Fig. 3). The relationship between the droop coefficient and ROCOF is established as follows

$$\begin{cases} K = K_{max} & df/dt < f'_{st} \\ K = (K_{max} - K_{min}) \Big/ \left[ \sqrt{1 + \left( \dfrac{f_{req\_rate}}{f_a} \right)^{2n}} \right] + K_{min} & \\ f'_{st} \leqslant df/dt < 0 & \\ K = K_{min} & 0 \leqslant df/dt \end{cases} \tag{15}$$

$K_{max}$ and $K_{min}$ are the upper and lower limits of the droop coefficient $K$, respectively, both are constants. $f_{req_rate}$is the frequency change rate of the system input, $f_a$ is the filter cutoff frequency, $n$ is the filter order, in this article $n = 5$.

### *D. Model of AM-VFAM Control Strategy*

The model of AM-VFAM control strategy comprises three VFAMs, three AMs, one synchronous generator, and static load components. To address the frequency regulation requirements arising from power imbalances, this paper proposes a primary frequency control strategy for load-side AMs, as illustrated in Fig. 4. This strategy quantitatively models the dynamic coupling relationship between frequency and power through a transfer function representation. Fig. 5 further demonstrates the implementation of this control strategy under a three-zone division framework.

where $M$, $D$, $T_R$, $F_H$, $K_m$, $K$, $R$, $\Delta P_D$, and $\Delta P_{DA}$ are equivalent inertia coefficient, equivalent damping coefficient, reheating time constant, high-pressure turbine fraction, coefficient related to the generator power factor, droop control coefficient of the VFAM, speed control coefficient of the speed regulator, unbalanced power and power reduction amount of the conventional AM participating in the response, respectively.

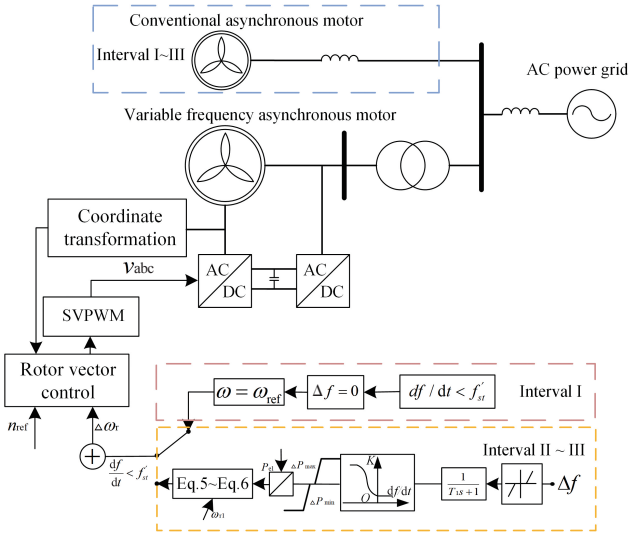


Fig. 5. Frequency response curve based on ROCOF division interval.

This strategy of segmenting the system frequency response according to the motor structure can maximize its contribution to the system frequency response while ensuring the normal operation of the motor.

where $\omega$, $\Delta\omega$, and $n_{\text{ref}}$ are the angular velocity, the angular velocity change, and the reference speed of the VFAM, respectively.

Fig. 5 is the variable droop control link of the VFAM, which is used to adjust the motor's power according to the system frequency deviation. The lower part is the conventional AM frequency response transfer function [28]. The signals in the figure interact through feedback and feedforward paths to achieve the adjustment of the system frequency deviation.

## IV. Power Control Strategy of MPC Based on Adaptive Weight Coefficient

Based on the concept of droop control, this paper introduces a variable-weight MPC rolling optimization strategy building upon segmented control. By dynamically adjusting the weight coefficients in traditional MPC, it responds in real-time to system frequency deviation and its rate of change, optimizes control parameters online, and ultimately achieves precise compensation of the VFAM input power by solving the objective function [29]. The block diagram of the frequency modulation control based on variable weight adaptive MPC proposed in this paper is shown in Fig. 6.

### *A. Construction of the MPC Model*

MPC is mostly used for digital control, and its discrete state expression is

$$\begin{cases} x_{k+1} = Ax_k + Bu_k + Lz_k \\ y_k = Cx_k \end{cases} \tag{16}$$

where $x(k+1)$, $x(k)$, $u(k)$, $w(k)$, $y(k)$, $A$, $B$, $C$, *and* $L$ are the state

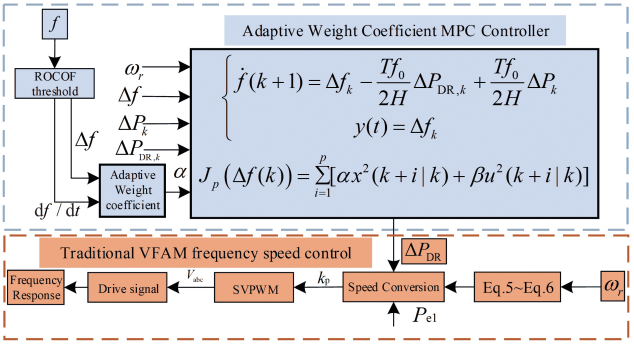


Fig. 6. Frequency modulation control block diagram of variable-weight adaptive MPC.

variables of the system at time $k$+1, system state variable at time $k$, input variable of the system, disturbance variable, output variable, system control matrix, the input control matrix, output control matrix, and the system disturbance matrix.

Based on the discretization formula, the system frequency can be expressed as

$$\begin{cases} \dot{f}(k+1) = \Delta f_k - \dfrac{Tf_0}{2H_s}\Delta P_{\text{DR},k} + \dfrac{Tf_0}{2H_s}\Delta P_k \\ y(t) = \Delta f_k \end{cases} \tag{17}$$

$\Delta f_k$ is the frequency difference of the system frequency at time $k$, $f_0$ is the rated frequency of the system, $T$ is the discrete-time constant, $\Delta P_{\text{DR},k}$ is the active power adjustment of the VFAM at time $k$, and $\Delta P_k$ is the unbalanced power of the power system at time $k$.

The coefficients of each matrix in the system are

$$\begin{cases} A = [1] \\ B = \left[-\dfrac{Tf_0}{2H_s}\right] \\ L = \left[\dfrac{Tf_0}{2H_s}\right] \\ C = [1] \end{cases} \tag{18}$$

### *B. Adaptive Weight Coefficient Design for MPC*

The weight coefficient represents the relative importance of the performance index in the optimization objective function, and its value is negatively correlated with the corresponding variable adjustment amplitude. This section designs a collaborative strategy MPC to dynamically optimize the frequency-power response trajectory of the VFAM through time-varying weight coefficient matrix.

$$w = w_1(\delta_f) + w_2(\delta_{f_{\text{rate}}}) \tag{19}$$

where $\delta_f$, $\delta_{f_{\text{rate}}}$, and $w$ are $\Delta f$, ROCOF, and weighted composite signal of $\Delta f$ and ROCOF, respectively. $w_1$ and $w_2$ are multi-objective weighting coefficients.

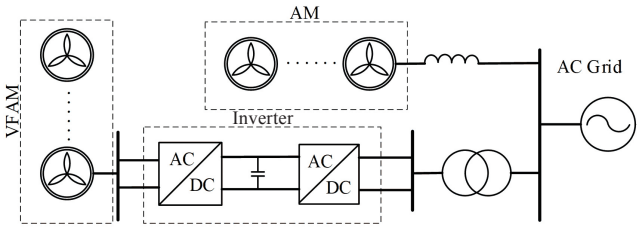


Fig. 7. Topological structure of the simulation system.

TABLE II
PARAMETERS OF THE SIMULATION SYSTEM

| Equipment | Parameter | Numeric Value |
|---|---|---|
| Synchronous motor | Rated power/kW | 2000 |
| | Rated voltage/V | 600 |
| | Stator resistance/Ω | 0.00076 |
| | *d*-axis reactance $X_d$/Ω | 0.165 |
| | *q*-axis reactance $X_q$/Ω | 0.121 |
| AM-VFAM | Rated power/kW | 110 |
| | Rated voltage/V | 400 |
| | Rated frequency/Hz | 50 |
| | Inertia time constant/s | 1.5 |
| | Viscous friction coefficient F/N·m·s | 0.05421 |
| | Mutual inductance/H | 0.01038 |
| $T_1$ | Filter time constant | 0.0866 |
| $K$ | $K_{max}$ | 28 |
| | $K_{min}$ | 6 |

$$\alpha = \begin{cases} w \cdot e^{k_1 \cdot (-w)} & w < 0 \\ \dfrac{w}{1 + e^{k_2 \cdot w}} & w \geqslant 0 \end{cases} \tag{20}$$

$$\beta = 1 - \alpha \tag{21}$$

where $k_1$ and $k_2$ are the sensitivity coefficient governing the steepness of the weight change, $\alpha$ and $\beta$ are weighting coefficients for frequency deviation and control action penalties, respectively.

The weighting matrix $Q$ in the quadratic performance index is structured as a block-diagonal matrix to decouple the state and input contributions in the cost function. Specifically, $Q$ is formulated as

$$Q = \mathrm{diag}(q_1, q_2, \cdots, q_p) \tag{22}$$

$$q_p = \begin{bmatrix} \dfrac{\alpha}{\Delta t^2} & 0 \\ 0 & \dfrac{\beta}{\sigma^2} \end{bmatrix} \tag{23}$$

where $\Delta t$ is the sampling interval, $\sigma$ is the normalization coefficient. The state weighting coefficient $\alpha$ is adaptively increased during high-frequency deviation or elevated ROCOF conditions to prioritize deviation suppression, while the input weighting coefficient $\beta$ is dynamically reduced under severe power disturbances to allow larger control inputs.

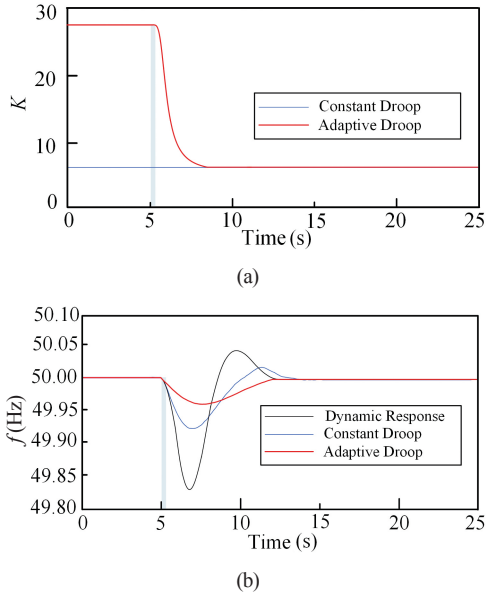


Fig. 8. Topological structure of the simulation system. (a) Droop coefficien, (b) System frequency.

The MPC also needs to consider the operating constraints of each unit during the control process. Therefore, the objective function incorporating the constraints of the VFAM is presented below:

$$\begin{cases} J_p\left(\Delta f(k)\right) = \sum_{i=1}^{p} [\alpha x^2(k+i\,|\,k) + \beta u^2(k+i\,|\,k)] \\ 0 \leqslant \left|\Delta P_{\mathrm{DR},\,k+i|k}\right| \leqslant \Delta P_{\mathrm{DR},\,max}, i = 0,1,2,\cdots,N-1_k \end{cases} \tag{24}$$

where $P_{m,k}$ is the power state quantity of the VFAM at time $k$, and $\Delta P_{DR,max}$ is the load capacity constraint value that can be decreased at the time of the VFAM.

## V. CASE STUDIES

To verify the effectiveness of the strategy proposed in this paper, a simulation system model as shown in Fig. 7 was built in Simulink. The system consists of a synchronous generator, AMs and VFAMs. Each AM and VFAM comprises a 50 kW static load and a drive with a torque constant of $T$ = 400 N·m, and is connected to the grid via a dedicated transformer and filter. The built simulation system is simulated and analyzed.

### *A. Simulation of Adaptive Droop Control With Segmented ROCOF*

When $t$ = 5 s, the load suddenly increases by 10% further. The frequency response of load-side variable droop control between ROCOF partitions in the power system is compared with the dynamic response without VFAM and with the traditional control strategy. The simulation results of Method 1 (traditional control strategy in constant droop control) and Method 2 (adaptive droop coefficient $K$ control) are compared, as shown in Fig. 8.

Fig. 8 demonstrates the system frequency response under

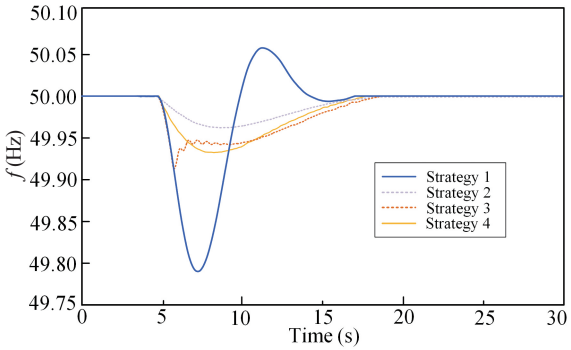


Fig. 9. System frequency in different $F_{st}$ thresholds.

three different control strategies when subjected to a 10% frequency disturbance. As shown in Fig. 8(a), the adaptive droop control maintains the $K$ value at its maximum during the initial disturbance stage to participate in system response and suppress frequency deviation. Fig. 8(b) reveals that under the same disturbance condition, the proposed adaptive weighting coefficient effectively responds to system frequency variations. When the system frequency reaches its nadir, the $K$ value decreases to its minimum level. This approach maximizes participation in system frequency response while enabling adaptive regulation of the asynchronous machine's rotor speed. In contrast, conventional droop control can only provide limited frequency regulation support and fails to adaptively maximize its involvement in system frequency response according to real-time frequency dynamics. The proposed method demonstrates superior frequency response performance compared to traditional droop control strategies, rapidly restoring the system frequency to the secure operational range after disturbance occurrence without compromising normal VFAM's operation.

### *B. Simulation Results Under Different $F_{st}$ Thresholds*

A comparative analysis of the simulation results for the proposed MPC-based strategy under different $F_{st}$ thresholds is presented in this paper. Given that the observed frequency variation of the system disturbance lies between ±0.2 Hz and ±0.3 Hz, the threshold is set accordingly to within 0.1 Hz. Strategy 1, Dynamic response without VFAM; Strategy 2, Proposed MPC with VFAM without threshold; Strategy 3, Proposed MPC with VFAM with $F_{st}$ = 0.06 Hz; Strategy 4, Proposed MPC with VFAM with $F_{st}$ = 0.03 Hz. The simulation results are presented in Fig. 9.

Fig. 9 illustrates the system frequency response under a 15% load disturbance to analyze the impact of different $F_{st}$ thresholds on VFAM's participation in frequency regulation. Upon detecting that the actual ROCOF reaches a threshold determined by (14) for a setting $F_{st}$, the control strategy (see Fig. 6) engages the MPC-driven VFAM to participate in the system response. As observed in the figure, a higher $F_{st}$ threshold delays the VFAM's response, resulting in a larger initial frequency deviation. Consequently, the system frequency nadir increases with the $F_{st}$ threshold. The power absorbed by the VFAM decreases as the $F_{st}$ threshold increases, indicating a relatively minor impact on the VFAM's own operation under moderate threshold values. Compared to the proposed MPC strategy without ROCOF consideration (see Strategy 2), this trade-off, which sacrifices part of the initial ROCOF response in exchange for reduced impact on the motor itself (see Strategy 4), helps balance the need to maintain the AM-VFAM's own rotational speed. However, an excessively high $F_{st}$ threshold can cause an abrupt change in the absorbed power, which in turn triggers a sharp decline in system frequency (see Strategy 3). Considering the inherent characteristics of the VFAM, simulation results indicate that the threshold setting of Strategy 4 in this paper not only ensures effective participation in system regulation but also mitigates its own impact to a certain extent.

TABLE III
COMPARISON OF FREQUENCY RESPONSE EFFECTS IN DIFFERENT CASES

| Case | Control Strategy | Frequency Nadir/Hz |
|---|---|---|
| Case 1 | Dynamic response without VFAM | 49.83 |
| | Conventional MPC with VFAM | 49.92 |
| | Proposed MPC with VFAM | 49.97 |
| Case 2 | Dynamic response without VFAM | 49.74 |
| | Conventional MPC with VFAM | 49.88 |
| | Proposed MPC with VFAM | 49.94 |

### *C. Simulation of MPC-Based Frequency Regulation Strategy With Segmented ROCOF*

The proposed MPC strategy for VFAM is compared with two benchmark control strategies, a conventional MPC strategy with VFAM, and a system without VFAM. The evaluation employs the parameters of test Scenario B, using the $F_{st}$ value as defined in Strategy 3. The system is subjected to two operating conditions: Case 1, a sudden 10% load increase at $t$ = 5 s, and Case 2, a subsequent sudden 20% load increase at $t$ = 5 s. The simulation results are presented in Fig. 10.

Fig. 10 and Table III present the results for Case 1 and Case 2, where the system is subjected to sudden load increases of 10% and 20%, respectively, at $t$ = 5 s. The comparative analysis, as summarized in Table III, leads to two key conclusions. First, the proposed MPC strategy effectively elevates the system frequency nadir (see Figs. 10(a) and 10(b)), outperforming the conventional MPC approach. Second, prior to the $F_{st}$ reaching its activation value, the proposed method yields a steeper initial ROCOF. The withheld initial response of the VFAM, a key feature of the control strategy, serves to minimize operational impacts.

As shown in Figs. 10(c) and 10(d), during the initial stage of an event, synchronous machine output change has a larger value in the proposed MPC than conventional MPC, the underlying reason is that the ROCOF during the initial stage has not yet reached the system threshold. Consequently, despite the large ROCOF magnitude, the VFAM remains inactive due to its $F_{st}$ constraint (see Figs. 10(e) and 10(f)), withholding its response until the predefined threshold is reached. Once this threshold is exceeded, the VFAM effectively participates in the

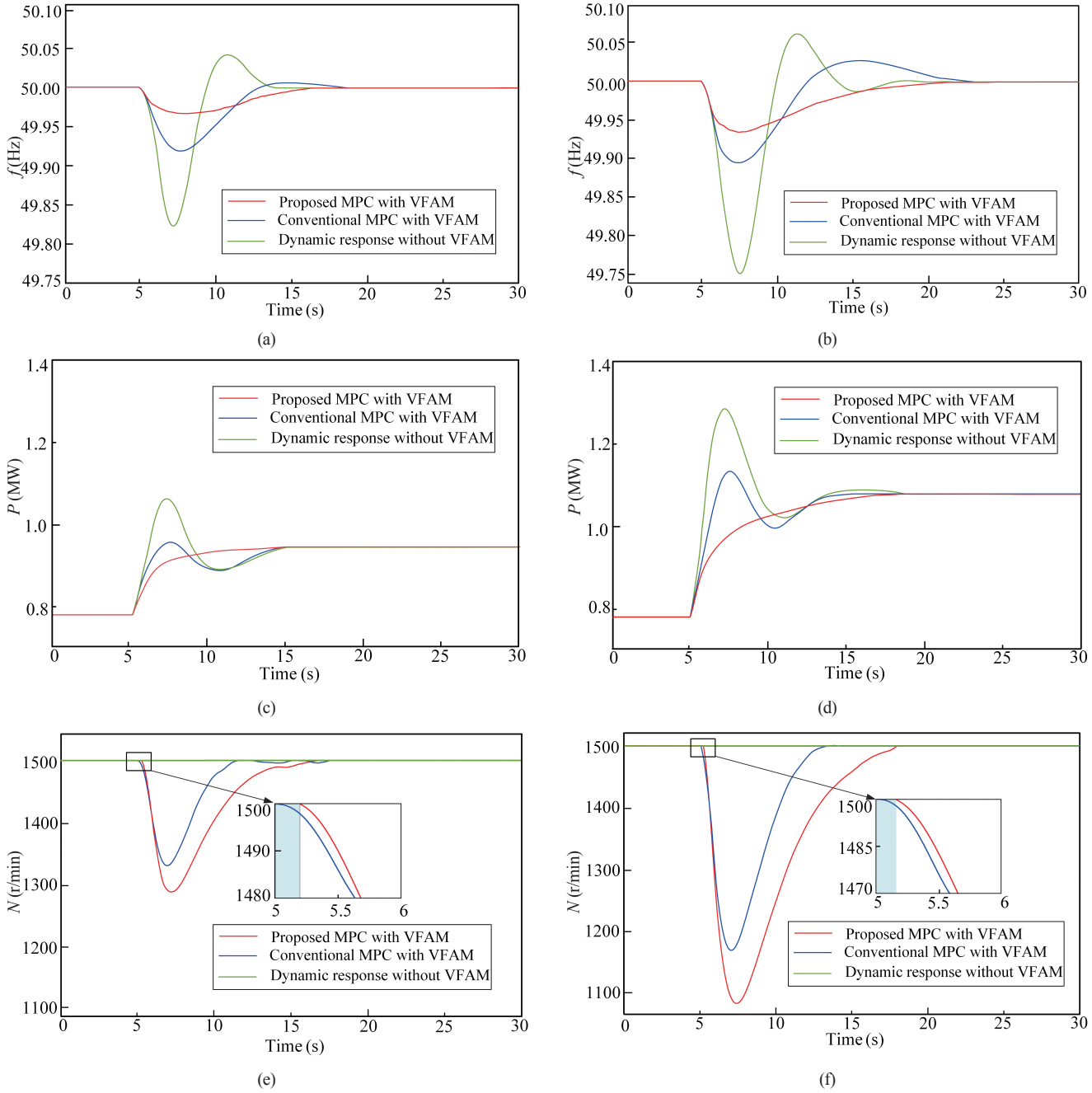


Fig. 10. Results for Case 1 and Case2. (a) Frequency of Case 1, (b)Frequency of Case 2, (c) Synchronous machine output change of Case 1, (d) Synchronous machine output change of Case 2, (e) Rotor speed of VFAM of Case 1, (f) Rotor speed of VFAM of Case 2.

system response and, upon reaching the maximum frequency deviation, initiates a recovery process that is more stable than that of conventional MPC. This is because of the adaptive weight coefficient of the proposed MPC, which can adaptively adjust according to the frequency deviation (see Figs. 10(e) and 10(f)). Note that the decrease $\omega_{r1}$ in proposed MPC is slightly larger than that in the conventional MPC. This helps a VFAM maintain sufficient capacity to handle a subsequent disturbance and ensure stable operation.

Table III shows the system frequency impact comparison between Case 1 and Case 2. In Case 1, the proposed strategy achieves an approximately 17% higher speed reduction in VFAM and improves the frequency nadir by approximately 29% relative to the baseline. Similarly, in Case 2, the speed reduction and frequency nadir improvement reach approximately 10% and approximately 23% respectively. By intentionally prolonging the speed restoration interval, VFAM achieves enhanced coordination with synchronous generators. This improves their frequency regulation participation while maintaining operational stability. Under the control strategy of this paper, in the simulation results of Case 1, the frequency is always maintained above 49.95 Hz; in Case 2, the frequency enters the safe domain earlier than the traditional frequency control strategy.

The above results demonstrate that the proposed scheme

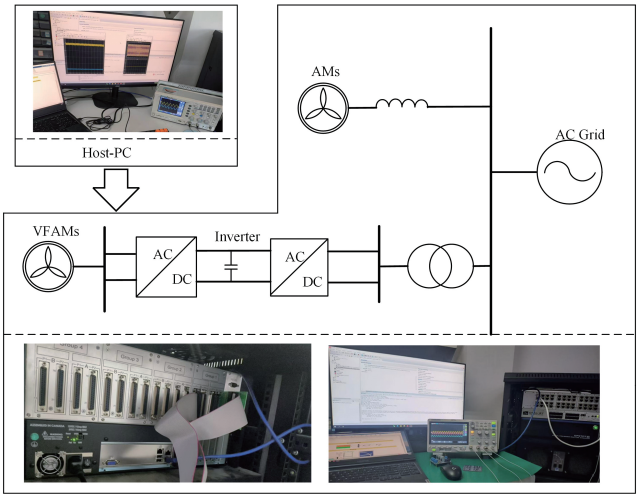


Fig. 11. VFAM modeled in HIL simulation platform.

successfully prevents the rotor speed of VFAM's $\omega_{r1}$ from reaching its minimum threshold. This is achieved by dynamically adjusting the control gain through real-time coordination of ROCOF and $\omega_{r1}$. The scheme remains effective even under disturbances such as sudden significant load increase events.

### *D. Performance Comparison With HIL Simulator*

The VFAM based MPC is modeled in OPAL-RT system as shown in Fig. 11, where the load part including AMs, VFAMs and static loads are simulated in OPAL-RT system. Comprehensive testing was conducted by analyzing frequency and motor speed variations under different $F_{st}$ settings in Scenario B. Additionally, the system's frequency response was specifically validated under the Case 1 operating condition. The simulation results are presented in Fig. 12.

Under a 15% sudden load increase in Scenario B, the HIL simulation results of the system frequency are presented in Fig. 12(a). The results indicate that the frequency responses of the four different strategies across various $F_{st}$ thresholds are consistent with those observed in Scenario B, thereby validating the feasibility of VFAM participation in frequency response under different $F_{st}$ thresholds. As observed, an increase in the $F_{st}$ threshold delays the participation timing of the VFAM in the system response and reduces the $\Delta P_{DR}$ to varying degrees. However, when the threshold exceeds a certain value, the motor speed drops abruptly, leading to increased adverse effects on the VFAM (see Fig. 12(b)). Additionally, under Operating Case 1 in Fig. 12(c), the proposed strategy's moderated speed recovery process successfully restores system frequency to a secure range, aligning with Scenario C findings.

## VI. Conclusion

This paper proposes a coordinated frequency response strategy integrating ROCOF interval division with adaptive MPC for power systems with high renewable penetration. The main findings are summarized as follows:

1) The proposed three-interval ROCOF framework effectively coordinates AMs and VFAMs. Conventional AM responds in the low ROCOF interval, while VFAM with dynamic droop coefficients is activated in medium-high intervals, enhancing frequency support while ensuring VFAM operational security. Experimental results demonstrate that the strategy proposed in this paper offers superior flexibility compared to the fixed-weight coefficient control for VFAM's participation in system response.

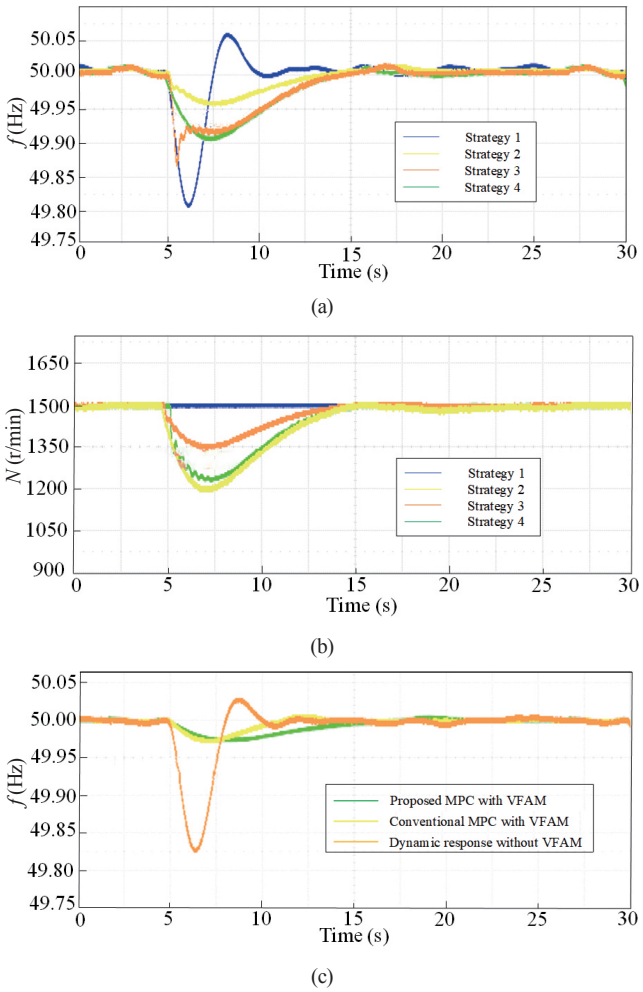


Fig. 12. Results for HIL. (a) Frequency for various $F_{st}$, (b) Rotor speed of VFAMs for various $F_{st}$, (c) Frequency of Case 1.

2) The adaptive-weight MPC controller demonstrates strong robustness under uncertainties. By dynamically adjusting weights, it maintains optimal frequency control performance under varying disturbances and system parameters. Compared to traditional MPC, the strategy proposed in this paper can better adapt to system frequency response under varying operating conditions.

3) Joint MATLAB/Simulink and HIL simulations verify that the proposed strategy offers marked improvements over conventional methods in both frequency nadir support and VFAM stability, demonstrating its effectiveness and practical viability.

## References

[1] D. A. Leiva Roca, P. Mercado, and G. Suvire, "System frequency response model considering the influence of power system stabilizers," in

*IEEE Latin America Transactions*, vol. 20, no. 6, pp. 912–920, Jun. 2022.
[2] B. Gundogdu, S. Nejad, D. T. Gladwin, M. P. Foster, and D. A. Stone, "A battery energy management strategy for U.K. enhanced frequency response and triad avoidance," in *IEEE Transactions on Industrial Electronics*, vol. 65, no. 12, pp. 9509–9517, Dec. 2018.
[3] M. Javadi, Y. Gong, and C. Y. Chung, "Frequency stability constrained BESS sizing model for microgrids," in *IEEE Transactions on Power Systems*, vol. 39, no. 2, pp. 2866–2878, Mar. 2024.
[4] P. V. Brogan, R. J. Best, D. J. Morrow, K. McKinley, and M. L. Kubik, "Effect of BESS response on frequency and RoCoF during underfrequency transients," in *IEEE Transactions on Power Systems*, vol. 34, no. 1, pp. 575–583, Jan. 2019.
[5] J. Ning, C. Jiang, Z. Zhang, Y. Zhang, L. Guo, P. Shi, and Y. Gu, "Thinking and technical practice of adjustable load resources participating in dispatching and control of power grid," in *Automation of Electric Power Systems*, vol. 44, no. 17, pp. 18, Sept. 2020.
[6] J. Ning, J. Wu, C. Jiang, Z. Zhang, Y. Zhang, and R. Xu, "Optimal control strategy of peak and frequency regulation for adjustable loads considering operation characteristics of resources," in *Automation of Electric Power Systems*, vol. 46, no. 15, pp. 11–19, Aug. 2022.
[7] Y. Sun, Z. Li, P. Xu, B. Li, B. Qi, Z. Liu, and X. Xie, "Research on key technologies and development direction of heterogeneous flexible load modeling and regulation," in *Proceedings of the CSEE*, vol. 39, no. 24, pp. 7146–7158, Dec. 2019.
[8] K. Samarakoon, J. Ekanayake, and N. Jenkins, "Investigation of domestic load control to provide primary frequency response using smart meters," in *IEEE Transactions on Smart Grid*, vol. 3, no. 1, pp. 282–292, Mar. 2012.
[9] Y. Tang, Z. Lu, and X. Fu, "Demand response strategies for promoting consumption of distributed power generation with residential active loads," in *Automation of Electric Power Systems*, vol. 39, no. 24, pp. 49–55, Dec. 2015.
[10] Y. Liu, Z. Wu, X. Lai, and D. Xu, "Cooperative control strategy for heterogeneous air-conditioning loads participating in frequency regulation of multi-area power systems," in *Power System Protection and Control*, vol. 53, no. 3, pp. 47–57, Feb. 2025.
[11] M. T. Muhssin, L. M. Cipcigan, N. Jenkins, S. Slater, M. Cheng, and Z. A. Obaid, "Dynamic frequency response from controlled domestic heat pumps," in *IEEE Transactions on Power Systems*, vol. 33, no. 5, pp. 4948–4957, Sept. 2018.
[12] X. Wu, J. He, Y. Xu, J. Lu, N. Lu, and X. Wang, "Hierarchical control of residential HVAC units for primary frequency regulation," in *IEEE Transactions on Smart Grid*, vol. 9, no. 4, pp. 3844–3856, Jul. 2018.
[13] K. Dhingra and M. Singh, "Frequency support in a micro-grid using virtual synchronous generator based charging station," in *IET Renewable Power Generation*, vol. 12, no. 9, pp. 1034–1044, Jun. 2018.
[14] Z. He, C. Wan, and Y. Song, "Frequency regulation from electrified railway," in *IEEE Transactions on Power Systems*, vol. 37, no. 3, pp. 2414–2431, May 2022.
[15] Y. Bao, J. Xu, S. Liao, Y. Sun, X. Li, Y. Jiang, D. Ke, J. Yang, and X. Peng, "Field verification of frequency control by energy-intensive loads for isolated power systems with high penetration of wind power," in *IEEE Transactions on Power Systems*, vol. 33, no. 6, pp. 6098–6108, Nov. 2018.
[16] Z. Luo, L. Nie, X. Tian, H. Wang, B. Li, and R. Ma, "Control strategy of electrolytic aluminum load participating in power network frequency stability based on model predictive control," in *Electric Power Construction*, vol. 44, no. 10, pp. 1–11, Oct. 2023.
[17] J. A. Aguado, A. J. Sánchez Racero, and S. de la Torre, "Optimal operation of electric railways with renewable energy and electric storage systems," in *IEEE Transactions on Smart Grid*, vol. 9, no. 2, pp. 993–1001, Mar. 2018.
[18] Z. Luo, X. Tian, X. Mo, L. Nie, X. Shen, and Y. Lei, "Frequency regulation of source-load-storage collaborative control with waste mine-pumped storage power stations," in *Power System Protection and Control*, vol. 52, no. 8, pp. 134–144, Apr. 2024.
[19] S. Nie, L. Chen, Y. Min, J. Zhang, F. Yin, J. Wu, and D. Cui, "Potential and characteristic analysis on participation of industrial load in primary frequency regulation," in *Power System Technology*, vol. 47, no. 10, pp. 3994–4004, Oct. 2023.
[20] T. Shimonishi, T. Mifune, and T. Matsuo, "Frequency-domain model order reduction of electromagnetic field in induction motor," in *IEEE Transactions on Magnetics*, vol. 58, no. 9, pp. 1–4, Sept. 2022.
[21] C. De Jonghe, B. F. Hobbs, and R. Belmans, "Optimal generation mix with short-term demand response and wind penetration," in *IEEE Transactions on Power Systems*, vol. 27, no. 2, pp. 830–839, May 2012.
[22] T. Liu, D. J. Hill, and C. Zhang, "Non-disruptive load-side control for frequency regulation in power systems," in *IEEE Transactions on Smart Grid*, vol. 7, no. 4, pp. 2142–2153, Jul. 2016.
[23] R. Azizipanah-Abarghooee and M. Malekpour, "Smart induction motor variable frequency drives for primary frequency regulation," in *IEEE Transactions on Energy Conversion*, vol. 35, no. 1, pp. 1–10, Mar. 2020.
[24] M. Malekpour, R. Azizipanah-Abarghooee, F. Teng, G. Strbac, and V. Terzija, "Fast frequency response from smart induction motor variable speed drives," in *IEEE Transactions on Power Systems*, vol. 35, no. 2, pp. 997–1008, Mar. 2020.
[25] A. Derviškadić, Y. Zuo, G. Frigo, and M. Paolone, "Under frequency load shedding based on PMU estimates of frequency and ROCOF," in *2018 IEEE PES Innovative Smart Grid Technologies Conference Europe (ISGT-Europe),* Sarajevo, Bosnia and Herzegovina, 2018, pp. 1–6.
[26] Y. Li, Z. Xu, J. Zhang, and K. Meng, "Variable droop voltage control for wind farm," in *IEEE Transactions on Sustainable Energy*, vol. 9, no. 1, pp. 491–493, Jan. 2018.
[27] S. K. Mishra, D. K. Upadhyay, and M. Gupta, "Approximation of fractional-order butterworth filter using pole-placement in W-plane," in *IEEE Transactions on Circuits and Systems II: Express Briefs*, vol. 68, no. 10, pp. 3229–3233, Oct. 2021.
[28] H. Zhang, C. Li, Y. Liu, Z. Huang, and K. Zhuang, "Review on power system dynamic frequency analysis and its application," in *Transactions of China Electrotechnical Society*, vol. 25, no. 11, pp. 169–176, Nov. 2010.
[29] B. Long, Y. Liao, K. T. Chong, J. Rodríguez, and J. M. Guerrero, "MPC-controlled virtual synchronous generator to enhance frequency and voltage dynamic performance in islanded microgrids," in *IEEE Transactions on Smart Grid*, vol. 12, no. 2, pp. 953–964, Mar. 2021.

**Yunlu Li** received the B.S. in Electronic Information Engineering from Shenyang University of Technology in 2009, the M.S. degree in Control Engineering in 2011, and Ph.D degree in Power Electronics and Drives from Northeastern University in 2017, Shenyang, China. He worked as a postdoctoral researcher at Shenyang University of Technology from 2017 to 2019. He worked as a guest researcher at the department of energy technology in Aalborg University, Denmark from 2018 to 2019. He is currently an Associate Professor in school of electrical engineering with Shenyang University of Technology, Shenyang, China.

His research interests include data-driven modeling of power system and renewable energy generation technology.

**Zhouying Liu** was born in 2001. She is currently studying Electrical Engineering at Shenyang University of Technology, pursuing the M.S. degree. Her research focuses on is the optimization control of load-side frequency regulation in power systems.

**Guotao Song** was born in 1999. He is currently studying Electrical Engineering at Shenyang University of Technology, pursuing the M.S. degree. His research focuses on is the optimization control of wind-storage combined frequency regulation.

**Jinliang Huang** was born in 1999. He is currently studying Electrical Engineering at Shenyang University of Technology, pursuing the M.S. degree. His research focuses on is microgrid modeling and renewable energy grid integration.